Solar light photocatalytic hydrogen production from water over Pt and Au/TiO$_2$(anatase/rutile) photocatalysts: Influence of noble metal and porogen promotion

Olivier Rosseler, Muthukonda V. Shankar [1], Maithaa Karkmaz-Le Du, Loïc Schmidlin, Nicolas Keller *, Valérie Keller

Laboratoire des Matériaux, Surfaces et Procédés pour la Catalyse – European Laboratory for Catalysis and Surface Sciences, CNRS-University of Strasbourg, 25 Rue Becquerel, 67087 Strasbourg Cedex, France

ABSTRACT

Hydrogen production from water under artificial solar light irradiation was performed over a series of Pt and Au/TiO$_2$(anatase/rutile) photocatalysts. Different TiO$_2$ supports with varying anatase/rutile contents were compared, based on either sol–gel synthesis or commercial TiO$_2$. The influence of template promotion on sol–gel TiO$_2$ synthesis has been studied using different porogens or templates. Among various factors influencing the hydrogen evolution efficiency, it was pointed out that the following parameters were crucial to enhance H$_2$ evolution: (i) the nature and content of the metallic co-catalyst, (ii) the surface, crystallographic, and porosity properties of the TiO$_2$ anatase/rutile support, (iii) the anatase/rutile ratio, (iv) the metal–support interactions, and (v) the relative amount of methanol added as a sacrificial reagent. The influence of these different factors was studied in detail. In optimized conditions, important H$_2$ production efficiency (120 μmol/min) was obtained over days without deactivation and with very low amounts of methanol.

© 2009 Elsevier Inc. All rights reserved.

1. Introduction

With increasing concern for the use of renewable resources and in particular for finding ways to use solar energy, solar light-activated photocatalysis is becoming an attractive tool. About 95% of the present hydrogen needs are covered by steam reforming of methane, a non-renewable source. Sustainable hydrogen production systems are of great importance for the future. Photocatalysis, with its potential to use sunlight for generating hydrogen, represents one of the promising technologies for clean and environmentally friendly hydrogen production and provides a way to use sunlight for generating hydrogen as a renewable green fuel. Photocatalysis, as opposed to other renewable energy production technologies, such as bio-fuel reforming, operates at ambient conditions without complex processing requirements. Since the discovery of photocatalytic water splitting on semi-conductor catalysts by Fujishima and Honda [1], efficient photocatalytic

hydrogen production, especially by direct water splitting is considered as a dream process because it enables pure hydrogen production from renewable sources without the application of an external potential. In the last years much effort has been put in the development of photocatalysts that are able to harvest solar energy and to convert it into chemical energy. More recently, several works have reported new photocatalysts with improved efficiency toward water splitting under solar light exclusively [2–6]. However, highly efficient hydrogen production by photocatalytic water splitting is still far from practical application and is closely linked to the development and improvement of nanomaterials.

The photocatalytic activity of TiO$_2$ can be increased or decreased by the presence of a noble metal co-catalyst deposited on its surface, depending on many factors such as the metal content and the nature of the reactant as well as the way of preparing the catalyst. The enhancement of the photocatalytic activity has been attributed to the formation of a Schottky barrier at the metal/semi-conductor interface, which leads to electron trapping and efficient charge separation [7]. Several metals have been tested and reported in numerous publications [8–13], emphasizing the best properties of the Pt/TiO$_2$ systems.

Some works performed in the last decades have shown that it was possible to increase the hydrogen production reaction rate for water splitting using water–alcohol mixtures, particularly water–methanol systems [13–17]. In these cases, the rate of hydrogen production was found to be much higher, compared to that obtained from photocatalytic cleavage of pure water. This increase has been attributed to the effect of the alcohol acting as a sacrificial agent (electron donor and holes and/or oxygen scavenger), by decreasing both electron–hole recombination and O_2/H_2 back reaction rates [18,19]. In most of these studies, the relative ratio of methanol to water was relatively high. Although this process is of interest in terms of environmental purposes and reduction in the use of fossil fuels, it still relies on a fossil-derived fuel, methanol or more generally on alcohols. A more sustainable route should involve either pure water splitting or water splitting assisted by lower amounts of methanol. Trying to lower and optimize the relative content of methanol while keeping high efficiency for water splitting is one of the goals of our study.

This work presents the results obtained for efficient photocatalytic hydrogen production on TiO_2 anatase/rutile-supported Pt and Au photocatalysts, including the search for optimized low ratio of methanol. The influence of both metals, on the one hand, and of the TiO_2 anatase/rutile-based support properties (anatase/rutile ratio, specific surface area, porosity, etc.), on the other hand, will be studied in detail and is correlated to complementary characterization methods. High rate of hydrogen production could be sustained over days without deactivation of the system on 0.3 wt.% Au/TiO_2 anatase–rutile photocatalyst.

2. Experimental

2.1. Material synthesis

The TiO_2 photocatalysts were based on the TiO_2–P25 standard from Degussa (now Evonik) with an anatase/rutile ratio of about 80/20 and a specific surface area of about 50 m^2/g, and sol–gel nanosized anatase/rutile template-promoted materials.

Nanosized sol–gel TiO_2-template-promoted photocatalysts were synthesized following a liquid phase low temperature dissolution–reprecipitation process using a sol–gel procedure in which the titanium isopropoxide was first hydrolyzed by the addition of a 2 M HCl aqueous solution, followed by a 48-h aging of the obtained hydrosol [20]. Even at room temperature aging, the thermodynamically stable rutile phase with fine particle size could be obtained [21]. The porogen template, polyoxyethylene(10)cetyl

ether (Brij 56), polyethylene glycol (PEG), polyvinyl alcohol (PVA), or hexadecyltrimethylammonium bromide (CTAB) was then added after the aging step and the reactant mixture was first dried at room temperature and then further dried at 110 °C before the final treatment in air at 400 °C for 2 h. Table 1 summarizes the different porosity promoters added during the sol synthesis and their main characteristics. The resulting samples are denoted TiO_2–Brij56, TiO_2–PEG, TiO_2–PVA, and TiO_2–CTAB, respectively. More generally, TiO_2-porogen-promoted samples will be denoted TiO_2-P.
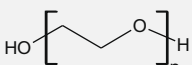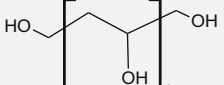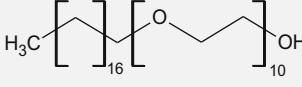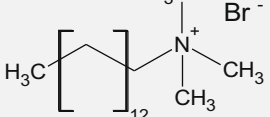
The platinum deposition was performed by wet impregnation using an aqueous solution of H_2PtCl_6. After drying at 110 °C for 1 h in air, and oxidation at 350 °C for 2 h, the material was finally reduced in flowing hydrogen at 350 °C for 1 h. Amongst many reported deposition methods [22], gold nanoparticle deposition was performed here following the Direct Anionic Exchange (DAE) method developed by Ivanova et al., which consists in hydroxyl surface groups exchange with gold complexes [23]. The TiO_2 support was immerged into an aqueous chloroauric acid solution ($HAuCl_4$) and was further heated at 70 °C for 1 h. The solution was subsequently washed with ammonia (35 vol.%) for 20 min, filtered, and the resulting material was further dried at 120 °C and calcined at 300 °C for 4 h in air (heating rate of 5 °C/min). In this deposition process, the pH range strongly influences the gold complex nature from $AuCl_4^-$ to $Au(OH)_4^-$ and the ammonia washing leads to gold complex grafting on the support surface by exchange with hydroxyl groups. The final calcination reduces the gold complexes to metallic gold nanoparticles.

2.2. Characterization techniques

Structural characterization was done by powder X-ray Diffraction (XRD) measurements, carried out on a D8-Advance diffractometer equipped with a Vantec detector, in a $\theta/2\theta$ mode using the Kα_1 radiation of Cu at 1.5406 Å. The rutile and anatase contents were derived from the intensity of the most intense diffraction peaks, the rutile (1 1 0) and anatase (1 0 1) peaks at 27.6° and 25.4°, respectively, according to the JCPDS files 21–1276 and 21–1275.

The surface area measurements were performed on an ASAP2010 Micromeritics porosimeter using N_2 as an adsorbent at liquid N_2 temperature. Prior to N_2 adsorption, the material was outgassed at 200 °C for 1 h in order to desorb impurities or moisture from its surface. The surface areas were calculated by applying the B.E.T. and t-plot methods.

Table 1
Different porogen promoters/templates used and added after the aging step during the sol–gel synthesis.

Name	Formula	Usual characteristics
PEG Poly(ethylene glycol)		Water soluble polymer used as thickener in cosmetics
PVA Poly(vinyl alcohol)		Non-ionic surfactant lubricant for contact lens
Brij56 Polyoxyethylene(10)cetyl ether		Amphiphilic surfactant stable in acid and basic media
CTAB Hexaecyltrimethylammonium bromide		Cationic amphiphilic surfactant

Scanning Electron Microscopy (SEM) was carried out on a Jeol JSM-6700F working at 3 kV voltage, equipped with a CCD camera. The sample was previously coated with gold and then deposited on a standard aluminum holder for observation.

Transmission Electron Microscopy (TEM) was performed on a Topcon 002B microscope working with a voltage of 200 kV and a point-to-point resolution of 0.17 nm. The sample was sonically dispersed in an ethanol solution for 5 min and a drop of the solution was deposited onto a copper grid covered by a holey carbon membrane for observation.

The XPS measurements were performed on a MULTILAB 2000 (TERMO) spectrometer equipped with Mg Kα anode ($h\nu$ = 1456 eV). Charging effects were corrected using the C_{1s} peak at 284.6 eV as a reference for the graphitic carbon. All the spectra were decomposed assuming several contributions, each of them having a Doniach–Sunjic shape and a Shirley background subtraction.

Thermal Gravimetry Analysis (TGA) was performed using a SETARAM thermo-analyser. Each sample was placed in a platinum crucible and heated from room temperature to 900 °C with a heating rate of 10 °C/min, using a 20/80 (v/v) O_2/N_2 mixture at 50 cm^3/min flow stream.

The UV–Vis absorption spectra of the materials were recorded on a Cary 100 Scan UV/Vis spectrophotometer (Varian).

2.3. Experimental device and procedure

The liquid-phase hydrogen production was carried out in a Pyrex reactor, equipped with a plunging quartz tube containing a 150 W metal halide lamp (solar light simulation) located vertically, under 500 mL/min nitrogen flow (Fig. 1). This lamp was simulating the solar illumination, with a very low UV-A content and a large part in the visible light range. The measured irradiance was 30 mW/cm^2. All the experiments were performed in the same irradiance conditions. This tube was surrounded by a water circulation in a cylindrical Quartz jacket, in order to avoid heating of the aqueous media. The reaction was performed under a 500 rpm mechanical stirring. Prior to any experiment, oxygen was removed by nitrogen flushing. The reaction products were analyzed *on-line* every 2 min by thermal conductivity detectors on a micro-gas chromatography (Model Agilent P200 Series) allowing detection and quantification of hydrogen, oxygen, CO, CO_2, and organics on 5A molecular sieve, OV1, PlotQ, and Stabilwax columns. The photocatalytic tests were performed using pure water as a hydrogen source, and methanol as a sacrificial additive agent for enhancing hydrogen production. Different methanol/water ratios have been tested, varying in the 0–25 vol.% range. For a better comparison, all the photocatalytic tests were carried out with 1 g of catalyst and 1 L of total liquid.

3. Results on Pt/sol–gel TiO$_2$ (anatase/rutile)-porogen modified, Pt/TiO$_2$-P

3.1. Characterization results of the sol–gel TiO$_2$-P supports

The compared Thermal Gravimetry Analysis (TGA) performed on TiO$_2$–Brij56, TiO$_2$–PEG, TiO$_2$–PVA, and TiO$_2$–CTAB samples after drying at 110 °C and calcination at 400 °C revealed that whatever the templates or porosity promoters used, they were completely eliminated after calcination (graphs not shown, see in [24] in the case of the TiO$_2$–PEG material). The exothermic heat evolution obtained on the dried samples indicated the combustion of the porogen below 400 °C, whereas this exothermic peak did not appear anymore on the samples calcined at 400 °C, confirming the removal of the porogen during the calcination step.

The nitrogen adsorption/desorption curves provided information related to the porous texture of the different porogen-modified samples, taking PEG, PVA, and Brij56 as examples (Fig. 2). All the TiO$_2$-P materials revealed type-IV isotherms, characteristic of mesoporous solids with a uniform pores distribution (even in the case of CTAB, not represented here). Fig. 2 represents the nitrogen adsorption/desorption curves of non-modified sol–gel TiO$_2$, exhibiting also type-IV behavior.

It has already been shown, using this low temperature dissolution–reprecipitation sol–gel process, that the thermodynamically stable rutile phase with a fine particle size appeared after 300 min of aging, even at room temperature [25]. Table 2 summarizes BET and XRD characterizations of the different TiO$_2$-P and unmodified samples, compared to the commercially available TiO$_2$–P25 reference. One could note that for a same aging duration, the nature of the template had a huge influence on the anatase/rutile ratio. More precisely, the addition of PEG porogen yielded the formation of a large ratio of the rutile phase (95%), whereas this proportion decreased in the order PVA (70%), CTAB (60%), and Brij56 (50%). Without the addition of a template, pure rutile phase was obtained, but with higher surface area than for usual rutile phase obtained by heating anatase phase at high temperature (30 m^2/g against 8 m^2/g), pointing out the interest of these low temperature sol–gel syntheses. The addition of template also delayed the anatase–rutile phase transition. It is also worth mentioning that crystallites obtained by this low temperature sol–gel synthesis exhibited a much lower size than in the case of the reference TiO$_2$–P25.

Adding a template during the low temperature dissolution–reprecipitation synthesis enhanced the specific surface areas, confirming that the templates acted as porogens or porosity promoters; this positive effect is induced by the template decomposition during the post-synthesis thermal treatment. The fingerprint, after decomposition of the porogen or template will, of course be specific, depending on both size and chemical nature. The corresponding measured specific surface areas ranged from 70 m^2/g (TiO$_2$–CTAB) to 190 m^2/g (TiO$_2$–PEG). The mean pore diameter values, in the 4–10 nm range confirmed the presence of mesopores and the influence of the nature of the porogen/template on the resulting pore sizes.

UV–Vis absorption spectra recorded for these sol–gel TiO$_2$-P-based samples were clearly shifted toward the visible light part of the spectrum (also called red-shift), compared to the reference TiO$_2$–P25 (Fig. 3). Whatever the template or porogen used, the absorption was extended up to 550 nm but is stronger in the 400–450 nm range. The graphical determination of the cut-off wavelengths was performed for estimating the band gap energy
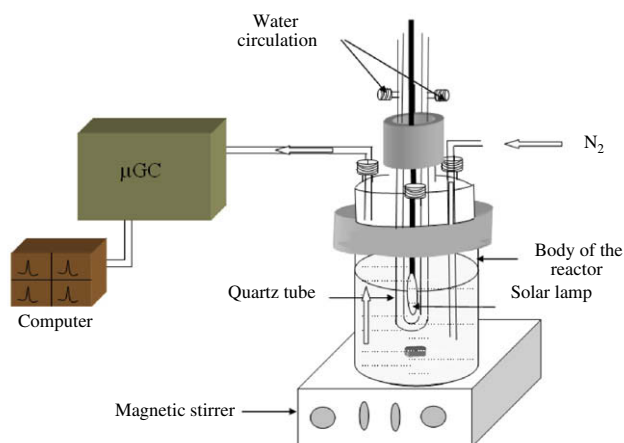

Fig. 1. Water-splitting photoreactor coupled with an *on-line* microGC.
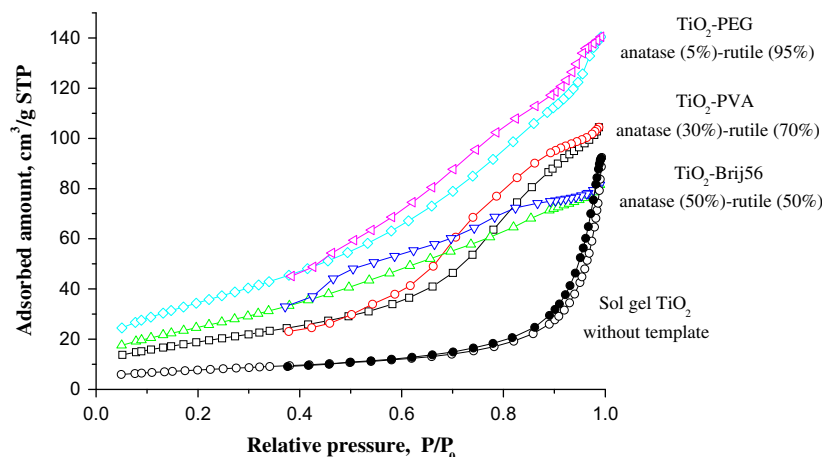
Fig. 2. Adsorption/desorption isotherms of sol–gel TiO$_2$-P modified samples. Examples of PEG, PVA and Brij56 as templates.

Table 2
Specific surface area, mean crystallite size diameter, anatase/rutile ratio, mean pore diameter and total porous volume, depending on the starting template after 48 h aging.

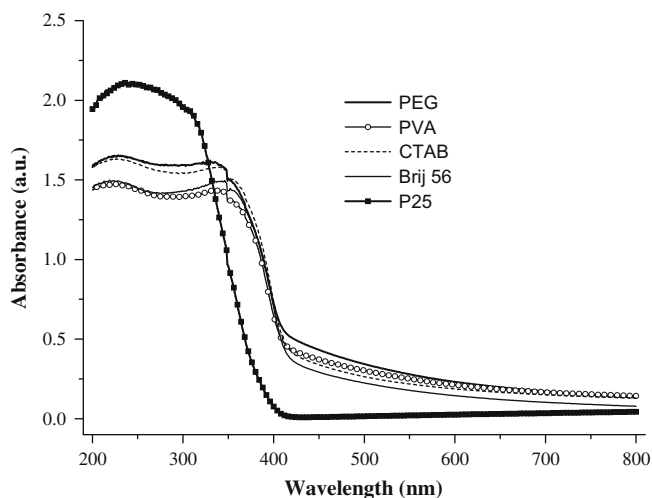| TiO$_2$	Surface area (m^2/g)	Crystallite size (nm)		Anatase:rutile ratio	Mean pore diameter (nm)/ porous volume (cm^3/g)
		Anatase	Rutile		
TiO$_2$–Brij56	100	7	10	50:50	10/0.35
TiO$_2$–PEG	190	–	11	5:95	4/0.64
TiO$_2$–PVA	150	9	10	30:70	4/0.28
TiO$_2$–CTAB	70	11	10	40:60	6–7/0.18
Without template	30	–	10	0:100	/
P25	50	32	52	80:20	/
P25 calcined at 800 °C	8	–	64	0:100	/

Fig. 3. Light absorption properties of TiO$_2$-P materials.

Table 3
Apparent band gap and cut-off wavelength of the different TiO$_2$ sol-gel-template-assisted materials.

Template	Band gap (eV)	Cut-off wavelength absorption (nm)	Anatase: rutile ratio
TiO$_2$–PEG	2.94	422	5/95
TiO$_2$–PVA	2.97	419	30/70
TiO$_2$–CTAB	2.99	415	40/60
TiO$_2$–Brij56	3.02	411	50/50

values, both summarized in Table 3. The calculated band gap energies were all close to 2.98 ± 0.04 eV. The higher the rutile content, the lower the apparent band gap energy (and the higher the cut-off wavelength), as expected. Although the effect of carbon doping on the visible light absorption is currently discussed in the literature, it appeared in our case very unlikely, whatever the porogen promoter used. Indeed, according to the TGA/TDA analyses, there was no carbon elimination (as CO$_2$) up to 900 °C. Consequently, one could assume that the shift in the visible light domain observed on the TiO$_2$-P samples was certainly due to the formation of the rutile phase, whose content was higher than that for TiO$_2$–P25. Furthermore, the addition of Pt (0.3 wt.% or 2 wt.%) to the sol–gel TiO$_2$-P samples did not change the UV–Vis absorption characteristics (not shown in Fig. 3).

SEM images showed particle aggregations to form uniformly sized 100–200 nm nanoclusters (Fig. 4, TiO$_2$–Brij56 given as an example), similar to that observed for the TiO$_2$–P25. According to XRD measurements, particle size ranged from 7 to 11 nm, depending on the templating agent. It should also be reminded that the porosity, measured previously in BET analyses, corresponds to open voids between particles within these aggregates.

High crystallinity of the particles, for both anatase and rutile phases, was confirmed by TEM analyses, showing nice and sharp fringes (Fig. 5); the measured 0.35 and 0.45 nm interplane distances corresponded to the anatase (1 0 1) and rutile (1 1 0) crystallographic planes, respectively [26].

To summarize, the above-described synthesis and characterizations of TiO$_2$ using a low temperature sol–gel method modified with different kinds of templates led to anatase–rutile composite semi-conductors and mesoporous materials showing high crystallinity and varying ratios of anatase/rutile phases. Depending on the
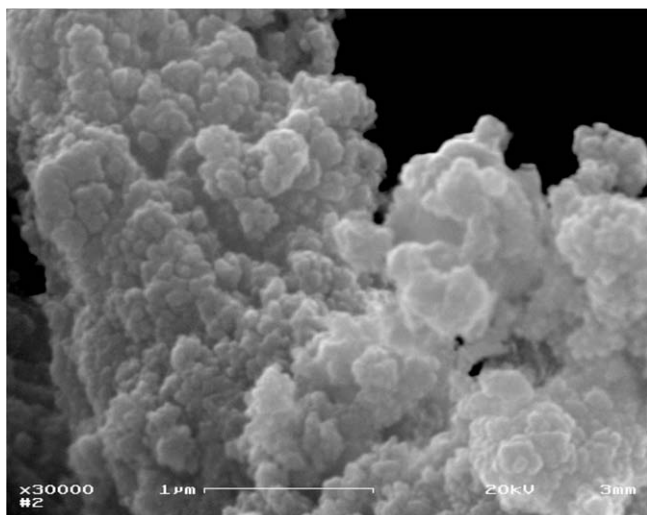
Fig. 4. SEM image of the sol–gel TiO₂–Brij56 material.

Fig. 6. On stream hydrogen production from methanol/water (250 ml/750 ml) mixture over 0.3 wt.% Pt/TiO₂-P and 0.3 wt.% Pt/TiO₂–P25 catalysts under artificial solar light illumination.

nature of the template added after the aging step during the sol–gel synthesis, both surface area (from 70 to 190 m²/g) and anatase/rutile ratio (from 5/95 to 70/30) could be tuned. The last parameter also had an influence on the band gap narrowing of TiO₂. The role of the different organic polymers acting as pore regulating agents has already been reported in the literature [27], pointing out the influence of their functional groups during the hydrolysis step of the synthesis. A more pronounced polarity could lead to stronger interactions with the surface of titania-based complexes and with the gel in solution. Hydrogen bond formation between templating agents and the growing titania particles in formation into the sol–gel have also been detected using IR spectroscopy. The different templating (amphiphilic, ionic, etc.) molecules with varying sizes and functional groups yielded self-assembly-like mesophases. Each template yields a specific mesophase, depending mostly on its size. During the drying step, these mesophases, trapped inside the TiO₂ network, were used as imprints. Finally, their elimination or decomposition during the calcination step led to the formation of potentially well-ordered mesoporous TiO₂, as reported in the literature [28].

3.2. Photocatalytic water splitting results

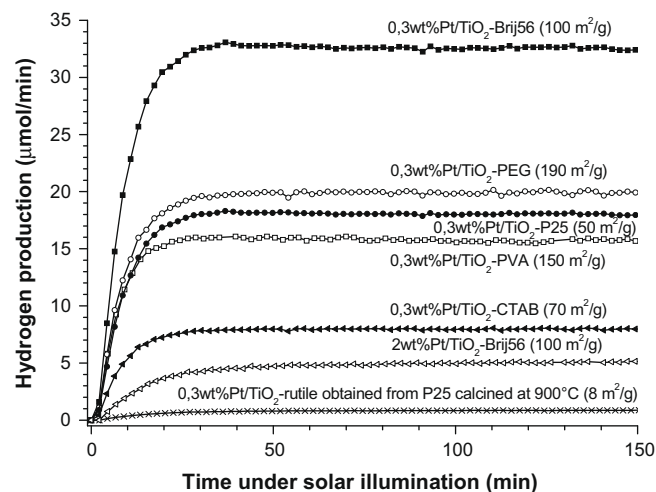Preliminary tests did not show any evidence of H₂ production from water without photocatalysts, neither in the dark, nor under illumination. Very negligible direct water splitting over bare TiO₂–P25 or TiO₂–P samples (<0.2 μmol/min) was recorded over a few minutes under illumination in pure water. Finally, it has been verified that methanol did not undergo photochemical decomposition, even for wavelengths lower than 300 nm, as already mentioned in the literature [29].

The different TiO₂–P supports were first compared at a given 25/75 methanol/water ratio to the reference TiO₂–P25 material. Fig. 6 summarizes the results obtained on the 0.3 wt.% Pt/TiO₂-P and 0.3 wt.% Pt/TiO₂–P25 samples, tested under the same conditions, keeping in mind that the only difference between the 0.3 wt.% Pt/TiO₂-P samples is the template used for enhancing the porosity. The results are nevertheless very different from one another. Amongst these samples, the 0.3 wt.% Pt/TiO₂–Brij56 exhibits the best efficiency (32 μmol/min or 1920 μmol/h), followed by the 0.3 wt.% Pt/TiO₂–PEG catalyst (20 μmol/min or 1200 μmol/h), both exhibiting higher activity than the 0.3 wt.% Pt/TiO₂–P25 reference sample (18 μmol/min or 1080 μmol/h). The 0.3 wt.% Pt/TiO₂–PVA (16 μmol/min or 960 μmol/h) and 0.3 wt.% Pt/TiO₂–CTAB (8 μmol/min or 480 μmol/h) samples showed the worst activities for hydrogen production. It must also be mentioned that the 0.3 wt.% Pt/TiO₂ rutile (100%) (obtained from calcined P25 at 800 °C) yielded very poor activity, certainly due to its low specific surface area (Table 2). Increasing the Pt content to 2 wt.% on the
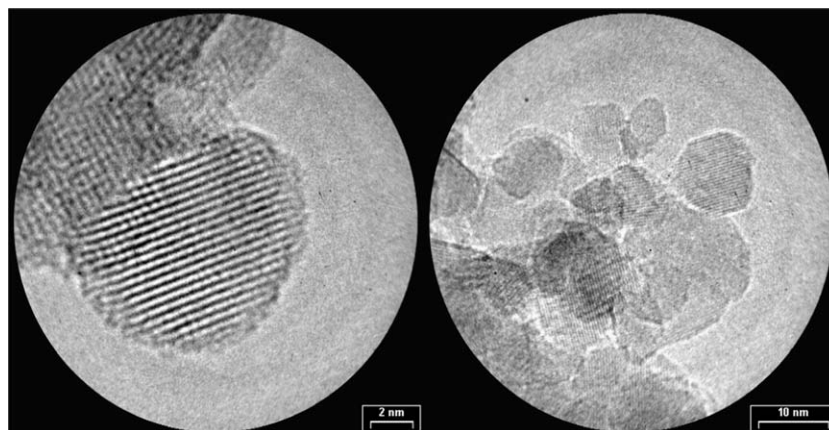

Fig. 5. TEM and high-resolution TEM (left) image of the sol–gel TiO₂–Brij56 sample. Example of an anatase particle (left) and of an anatase/rutile mixture (right).

Table 4
Hydrogen evolution rate (μmol min^{-1}) on 0.3 wt.% Pt/TiO$_2$–Brij56 as a function of the ratio of methanol sacrificial reagent. Stabilized value over more than 42 h of reaction.

Stabilized hydrogen evolution rate (μmol min^{-1})	Methanol volume (mL)	Methanol ratio (vol.%)
0.2	0.1	0.01
0.2	1	0.1
1	10	1
4	50	5
13	100	10
32	250	25

most efficient Pt/TiO$_2$–Brij56 sample, led to a decrease in photocatalytic H$_2$ production to very poor values. The same tendency could

also be underlined on the TiO$_2$–P25 reference, confirming previous observations that the optimum Pt loading lies in the 0.1–1 wt.% range [8,12,30–32]. This optimum in Pt content is often explained as the result of a competition between, (i) a decrease of electron/hole recombination at the TiO$_2$ surface in intimate contact with Pt (due to the electron trapping effect on Pt clusters) and (ii) electron/hole recombination on Pt. In addition, above a certain metal loading, the particles begin to touch and overlap, thus decreasing the metal–TiO$_2$ interface and the efficiency of charge transfers.

The steady-state regime of H$_2$ evolution is reported in Table 4 as a function of the methanol/water ratio, ranging from 0.01 to 25 vol.%, over the most active 0.3 wt.% Pt/TiO$_2$–Brij56 catalyst. It has already been illustrated in Fig. 6 that steady-state regime was reached for 25 vol.% of methanol after about 40 min under flow and illumination. No deactivation was observed over more
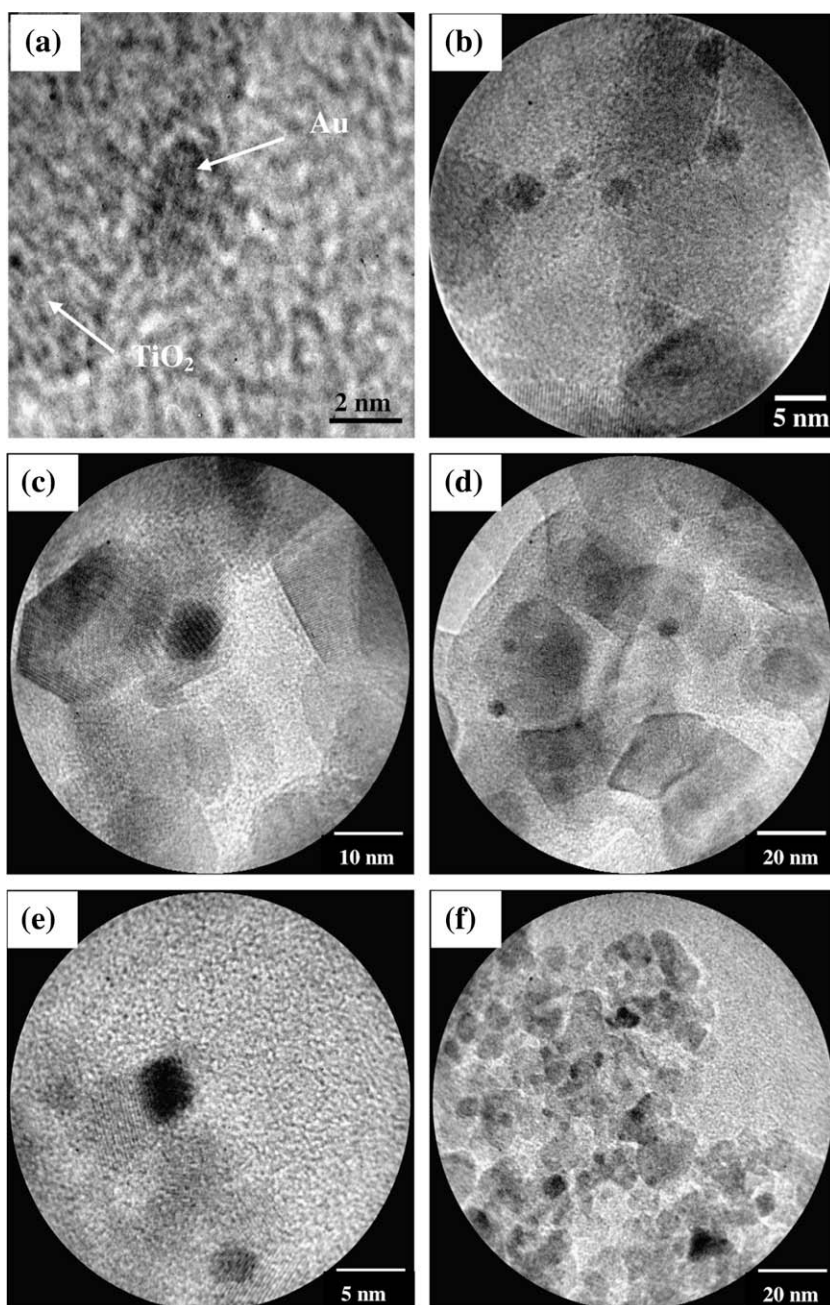

Fig. 7. TEM images of 0.3 wt.% Au/P25 (a) and (b), 2 wt.% Au/P25 (c) and (d), 2 wt.% Au/TiO$_2$–Brij56 (e) and (f) samples.

than 43 h of continuous reaction. The stabilized H_2 evolution rate was clearly enhanced by increasing the ratio of methanol sacrificial reagent.

The increase in photocatalytic activity for H_2 evolution over the 0.3 wt.% Pt/TiO_2–Brij56 photocatalyst could be explained putting forward different possibilities: (i) a higher Pt dispersion due to the higher porosity of TiO_2 after the removal of the template, resulting in better electronic interactions between the Pt co-catalyst and the support [33]; and (ii) the higher surface area, the higher the accessibility of the reactants to the actives sites; (iii) coupling both anatase and rutile particles enhances charge separation and takes advantage of the activation of the rutile in the visible region of the spectrum. In addition, as the evolution of H_2 and O_2 is expected to occur on different sites, on Pt/ anatase and rutile particles, respectively, it should limit the thermodynamically favored reverse reaction between O_2 and H_2, as already mentioned by other authors [34]. This could contribute to a certain extend to the higher activity of the TiO_2–Brij56 sample. Nevertheless, surface area and pore volume or distribution are obviously not the only factors affecting the photocatalytic activity but the anatase/rutile ratio also has to be considered. For example, TiO_2–PEG and TiO_2–PVA have the two largest surface areas (and TiO_2–PEG the highest pore volume) and also the highest rutile content with 95% and 70%, respectively. Consequently, a large rutile content, even though it absorbs a larger part of visible light, is detrimental to a high photocatalytic activity. As a result, anatase/rutile coupling and intimate contact in an optimal ratio allows (i) the absorption of a part of the visible light spectra via the rutile phase, by the so-called "antenna effect" in photocatalysis [35,36], (ii) the spatially separate evolution of H_2 and O_2, and (iii) the coupling, via hetero-junction formation, of two semi-conductors, anatase and rutile TiO_2, leading to a better separation of photogenerated charges through interparticle charge transfer [37–40]. The anatase–rutile semi-conductor coupling under solar light irradiation (UV-A + visible radiations) underlines the importance of the relative position of the valence and conduction bands of both semi-conductors. Anatase particles can only be activated by the small UV-A fraction of the solar irradiation, whereas rutile particles on the other hand can absorb the UV-A illumination but, in addition, are also able to absorb visible light up to 420 nm. When these two TiO_2 phases are in contact and simultaneously illuminated with solar light, both anatase and rutile semi-conductors can be activated at the same time, resulting in a vectorial photogenerated charge transfer and thus in a better charge separation. The more intimate the contact between anatase and rutile nanoparticles, the more efficient the electon/hole interparticle transfer phenomenon. But considering that anatase sites, or more precisely Pt/anatase sites, are the active sites for hydrogen evolution, a too high rutile content is therefore detrimental to hydrogen evolution. This assumption may explain the existence of an optimum anatase/rutile ratio.

4. Results on Au/TiO₂-P samples

Two kinds of supports have been evaluated for gold deposition and photocatalytic water splitting experiments, the above-mentioned TiO_2–Brij56, that showed the best results with platinum promotion, and the reference TiO_2–P25.

4.1. Characterization results

In addition to the previous characterizations of the TiO_2 supports (Section 3.1) in terms of TGA, BET, UV–Vis absorption, XRD, and SEM and TEM analyses, additional analyses have been further performed after gold deposition (UV–Vis absorption, BET measurements, and XRD and XPS analyses), for metal loadings varying between 0.3 and 2 wt.%.

Fig. 7 represents TEM images of 0.3 wt.% Au/TiO_2–P25, 2 wt.% Au/TiO_2–P25, and 2 wt.% Au/TiO_2–Brij56 photocatalysts at different magnifications. First, increasing the gold amount from 0.3 to 2 wt.% on TiO_2–P25 led to an increase in the mean particle size from 3 to 8 nm (Fig. 7a–d), however maintaining a high dispersion of the metallic nanoclusters. The same tendency is observed on TiO_2–Brij56, showing mean gold particle size of about 8 nm at 2 wt.% Au loading (Fig. 7e and f). It could be pointed out that although the surface area of the TiO_2–Brij56 support was two times larger, the metallic mean particle size was very similar at 2 wt.% content on both TiO_2–Brij56 and TiO_2–P25 supports, in spite of the higher dispersion expected on the former support.

UV–Vis light absorption spectra, after gold deposition, showed a modification of the absorption properties of TiO_2–P25 and TiO_2–Brij56 supports (Fig. 8). Unlike platinum, gold deposition mainly yielded an additional absorption band around 550 nm. Qualitatively, directly after gold deposition the sample had a much darker color (dark violet to almost black). Obviously, this colored material necessarily absorbs visible light, confirmed by the presence of a broad absorption peak centered around 550 nm. This absorption has already been reported in the literature and is attributed to a plasmon resonance phenomenon [41,42] due to collective oscillations of the conduction electrons located on the 6s orbital of gold and induced by the incident electromagnetic wave. This phenomenon is frequently observed for particle sizes between 5 and 50 nm, the absorption band width theoretically depending on the particle size. In addition to this plasmon absorption, deposition of gold also shifted the absorption spectrum deeper into the visible light range, in the 380–450 nm region. Consequently, the estimated band gap value was decreased (Table 5). The band gap narrowing could be as large as 0.33 eV or even 0.67 eV on TiO_2–Brij56 and TiO_2–P25 supports, respectively. Thus, regarding only that visible light absorption shift, without consideration of the plasmon resonance phenomenon, the addition of 1.4 wt.% of gold seemed to be the optimum ratio and led to the best absorption properties, whatever the TiO_2 support be.

For both TiO_2 supports and any gold content (between 0.3 and 2 wt.%), XRD characterizations did not show any diffraction peak characteristic of gold, certainly due to the low gold content, below detection limit. Furthermore, the results of BET and pore distribution analyses before and after gold deposition are not significantly different, meaning that such low gold concentrations do not affect
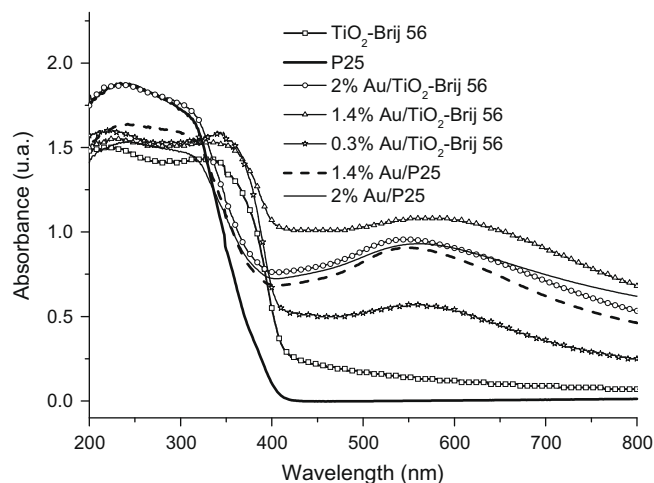

Fig. 8. Light absorption properties of Au/TiO_2 photocatalysts.

Table 5
Band gap and cut-off wavelength absorption of the different Au/TiO₂ anatase–rutile photocatalyst.

Photocatalyst	Band gap (eV)	Maximum wavelength absorption (nm)
P25	3.23	385
TiO₂ Brij56	3.02	411
1.4 wt.% Au/P25	2.69	461
2 wt.% Au/P25	2.76	450
0.3 wt.% Au/TiO₂ Brij56	2.91	427
1.4 wt.% Au/TiO₂–Brij56	2.56	485
2 wt.% Au/TiO₂ anatase–Brij56	2.73	455

the specific surface area, nor the pore size or distribution by filling or blocking them.

XPS characterizations have been performed on both TiO₂–P25 and TiO₂–Brij56 supports before and after gold deposition. For all these samples, Ti $2p$ (Fig. 9a), O 1 s (Fig. 9b and c), and Au $4f$ (Fig. 9d) spectra have been recorded, deconvoluted, and analyzed. The Ti $2p$ XPS spectra reported in Fig. 9a showed a signal that could be fitted with only two components, related to the Ti $2p$ spin–orbit components of Ti(IV) surface species. A first comparison between the two kinds of supports revealed a consistent binding energy shift of 0.7 eV. The Ti $2p^{3/2}$–Ti $2p^{1/2}$ spin–orbit components appeared at 458.0–463.7 and 458.7–464.2 eV for TiO₂–P25 and TiO₂–Brij56, respectively. This shift to higher binding energies observed on the sol–gel–Brij56-promoted support results from a different chemical environment of Ti(IV), compared to TiO₂–P25 and

more precisely from an increase in effective positive charges around Ti(IV). No contributions corresponding to Ti lower oxidation states have been detected. It can also be supposed from Fig. 9a that for both supports, the addition or grafting of gold by anionic exchange did not modify the Ti(IV) binding energies, evidencing that there is no direct interaction between gold and titanium atoms on the surface; indeed, no shift is detected for Ti 2p on 1.4 wt.% Au/TiO₂–P25 and 2 wt.% Au/TiO₂–Brij56. The very slight binding energy shift (about 0.2–0.3 eV) on 2 wt.% Au/TiO₂–P25 is not significant, compared to the experimental error to conclude an interaction or bonding between Ti and Au atoms.

The O 1 s region of the XPS spectra (Fig. 9b and c) exhibited a broad signal that has been deconvoluted into two contributions, a dominant peak at lower binding energy, corresponding to oxygen bonded to titanium atoms [43], and a weaker contribution, assigned to –OH surface hydroxyl groups at higher energy. The binding energy of the oxygen bonded to titanium contribution is located at 529.1 and 529.6 eV on TiO₂ P25 and TiO₂–Brij56, respectively (Fig. 9b). This difference in binding energy between the two supports is increased to 1 eV in the case of the –OH surface group contribution, identified at 530 and 531 eV, respectively. Gold deposition increased strongly this –OH surface contribution binding energy on TiO₂–P25 sample, showing a shift from 530 to 531.7 eV (Fig. 9c). In contrast, the addition of gold did not modify the position of the –OH contribution for the TiO₂–Brij56 sample. Furthermore, gold deposition also decreased the relative contribution of surface –OH groups, this effect being stronger on TiO₂–P25 than on TiO₂–Brij56. The –OH contribution on TiO₂–P25 decreased from 38% on the bare support to 19% and 12% after deposition of 1.4 and
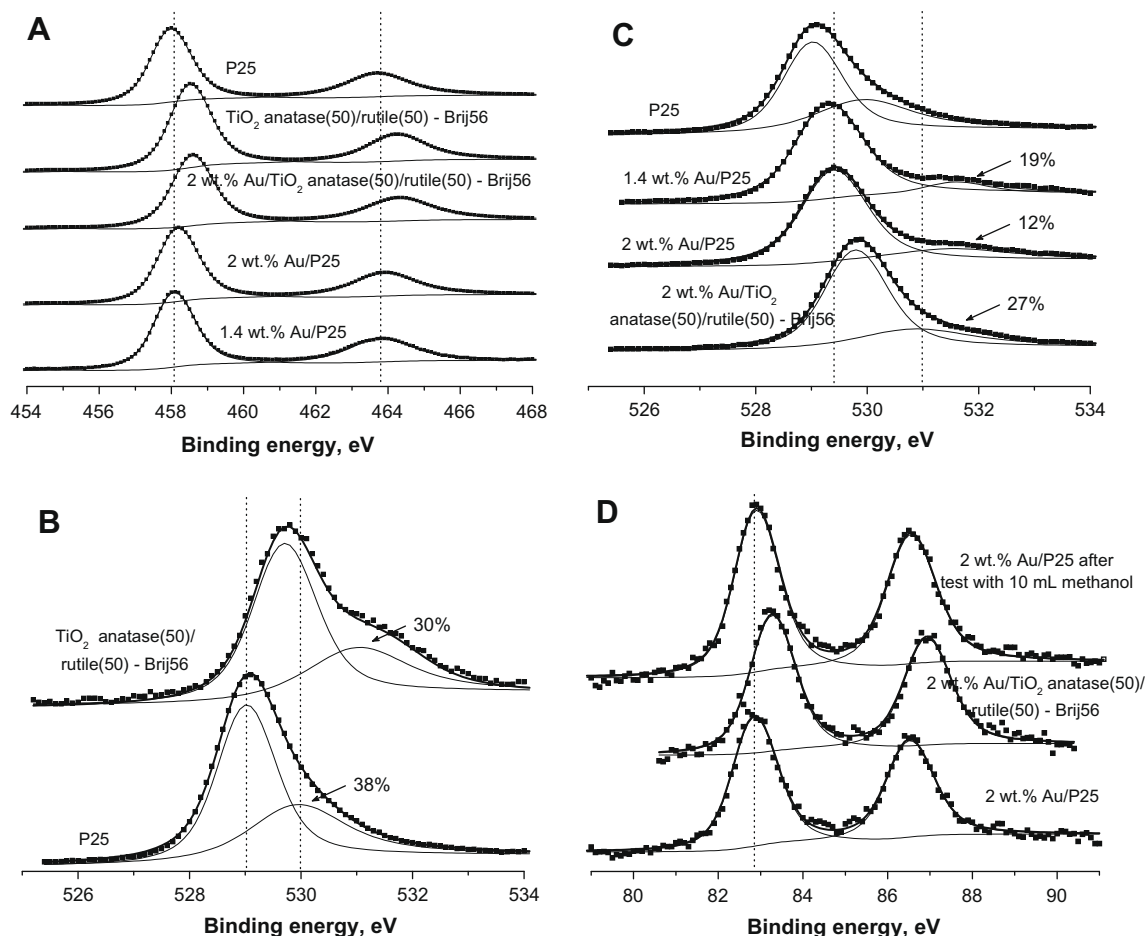

Fig. 9. XPS spectrum of (A) the Ti $2p^{1/2}$–Ti $2p^{3/2}$ region, (B) the O 1 s region of Au-free TiO₂, (C) the O 1 s region of Au/TiO₂, and (D) the Au $4f^{7/2}$–Au $4f^{5/2}$ region.

2 wt.% of gold, respectively, whereas it was only reduced from 30% to 27% on the TiO$_2$–Brij56 support after the deposition of 2 wt.% of gold. It must be underlined that gold deposition did not induce any shift in the position of the first contribution (i.e. oxygen bonded to titanium atoms). The strong intensity decrease and the large shift in binding energy of the second peak, on TiO$_2$–P25, suggest a direct coordination of gold atoms with the –OH surface groups. Indeed, during the ammonia washing step of DAE, gold complexes in solution are transformed into $[Au(OH)_4]^-$ and the complexed hydroxyls are then exchanged with surface –OH groups. The same interaction on TiO$_2$–Brij56 may not occur, or not be so strong, explaining the much lower decrease of the –OH signal.

The presence of metallic gold was confirmed on both kinds of support by the XPS spectra of Au 4f$^{7/2}$ and Au 4f$^{5/2}$ for 2 wt.% loading (Fig. 9d). Nevertheless, a 0.4 eV shift was observed between the two kinds of support, exhibiting binding energies of 82.9 and 83.3 eV, for TiO$_2$–P25 and TiO$_2$–Brij56, respectively. This shift clearly evidences different chemical environments and interactions with surface gold atoms. Based on the previous observation that, after gold deposition, mostly the –OH surface contribution of the TiO$_2$–P25 support was affected, it could be assumed that a specific Au–OH interaction or bonding occurs with this support. This is apparently not the case with the TiO–Brij56-promoted support.

Fig. 9d also shows that the photocatalytic test does not affect the oxidation state of gold on the 2 wt.% Au/TiO$_2$–P25 catalyst.

4.2. Photocatalytic water splitting results

Firstly, without the addition of methanol as a sacrificial reagent the pure water splitting efficiency of different Au/TiO$_2$ photocatalysts, previously characterized, was compared (Fig. 10). In contrast to Pt co-catalyst, only the TiO$_2$–P25 support led to H$_2$ production. However, on this TiO$_2$–P25 support, the hydrogen production rate was very low, whatever the samples tested (less than 0.25 μmol/min), and dropped to zero after relatively short periods. Besides, this decrease in H$_2$ production is faster on Pt-containing catalyst, compared to the equivalent gold catalyst. This faster deactivation is probably due to a more rapid poisoning of the active sites which may result from oxygen species strongly adsorbed on the surface of the metallic nanoparticles. Consequently, competitive side reactions are becoming predominant with time on stream: oxygen reduction by photogenerated electrons to form O$_2^-$ and O$_2^-$ oxidation by photogenerated holes [44]. Nevertheless, comparing the
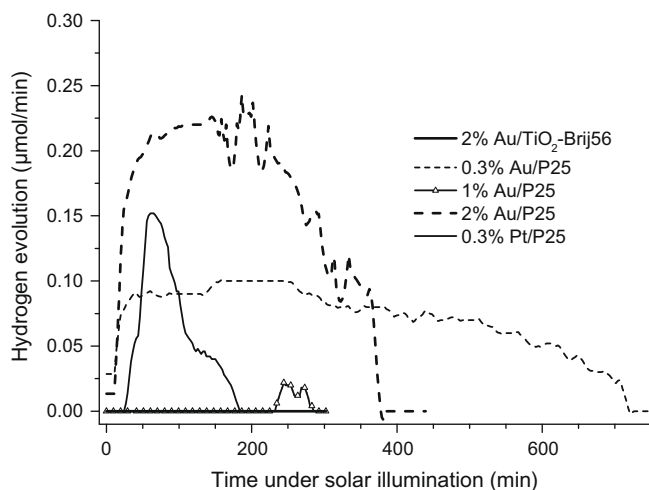

Fig. 10. On stream H$_2$ production from pure water on Au, Pt/TiO$_2$–P25, and 2 wt.% Au/TiO$_2$–Brij56 catalysts under artificial solar light illumination.

results obtained in Fig. 10 on Au/TiO$_2$–P25 with different gold contents (0.3, 1.4, and 2 wt.%), the optimal gold loading seems to be at 2 wt.%. It led both to the highest H$_2$ evolution rate and to the lowest deactivation, even if the H$_2$ production efficiency still remained very low, around 0.23 μmol/min. We could also notice that hydrogen production was close to zero on the 1.4 wt.% Au/TiO$_2$–P25 sample. On the 0.3 wt.% Au/TiO$_2$–P25 photocatalyst, despite the less important deactivation, the initial H$_2$ production efficiency was lower (Fig. 10). According to these preliminary tests, the 2 wt.% Au/TiO$_2$–P25 photocatalyst has been chosen for further photocatalytic tests, investigating the influence of methanol as a sacrificial reagent.

Fig. 11 summarizes the effect of the relative ratio of methanol sacrificial reagent on the 2 wt.% Au/TiO$_2$–P25 photocatalyst, compared to the 0.3 wt.% Pt/TiO$_2$–Brij56 sample, previously identified as the most efficient Pt-containing photocatalyst for H$_2$ production. Comparing these two series of Au- and Pt-containing photocatalysts, the results clearly indicate that the addition of methanol has a more beneficial effect for H$_2$ production on 2 wt.% Au/TiO$_2$–P25 catalyst. The addition of 1 vol.% (10 mL in 1 L) of methanol enhanced H$_2$ evolution by several orders of magnitude (from 0.23 μmol/min to 7200 μmol/h). Taking the last photocatalyst, for example, a long lasting experiment yielded, after 10 days of continuous reaction on stream, 38.7 L (1.728 mol) of H$_2$ production without deactivation. Of course, it is well known that under anaerobic conditions, methanol can also undergo photocatalytic reforming to produce hydrogen, according to Eq. (1) [12,45,46]. This means that the origin of the produced H$_2$ is therefore uncertain and may not be issued exclusively from photocatalytic water splitting. After 10 days of photocatalytic reaction with 10 mL of methanol (corresponding to 0.248 mol), the total detected amount of H$_2$ was 1.728 mol. Nevertheless, methanol reforming could have produced at best 0.744 mol of H$_2$. Thus, the total amount of the produced H$_2$ over 10 days exceeded the total amount that methanol reforming alone could provide (by a factor 2.3), evidencing that a large part of H$_2$ was undeniably produced by photocatalytic water splitting.

$$CH_3OH + H_2O \rightarrow CO_2 + 3H_2 \tag{1}$$

Consequently, the major part of methanol acts as an effective sacrificial reagent by scavenging either O$_2$ or holes, limiting the reverse H$_2$ + 1/2 O$_2$ → H$_2$O reaction, and increasing charge separation [47], respectively. In the former case, one may thus consider the photooxidation reaction of methanol, as expressed in Eq. (2).

$$CH_3OH + 3/2 O_2 \rightarrow CO_2 + 2H_2O \tag{2}$$

Assuming that methanol scavenges all the O$_2$ molecules produced through Eq. (3), i.e. 0.864 mol, the required quantity of methanol, according to Eq. (2) is 0.576 mol, which is about 2 times as much as the volume of the added methanol (0.248 mol).

$$H_2O \rightarrow H_2 + 1/2 O_2 \tag{3}$$

As the initial amount of methanol was only 0.248 mol, two explanations can be put forward: (i) H$_2$ production observed is not exclusively the result of water splitting but a part of it comes from methanol reforming and/or (ii) only a part of methanol is used to react with the O$_2$ produced through water splitting, the other part acting as hole scavengers. Table 6 summarizes the products continuously detected under steady-state conditions. The rates of O$_2$ and CO$_2$ evolution are constant and non-negligible. From the presence of O$_2$ in the outlet gas, the second hypothesis assuming that methanol photocatalytic oxidation does not consume all the O$_2$ produced can be confirmed. It also proves that H$_2$ and O$_2$ are efficiently separated on Pt/anatase and rutile, respectively. It must be reminded that O$_2$ is produced by water oxidation by holes (Eq.
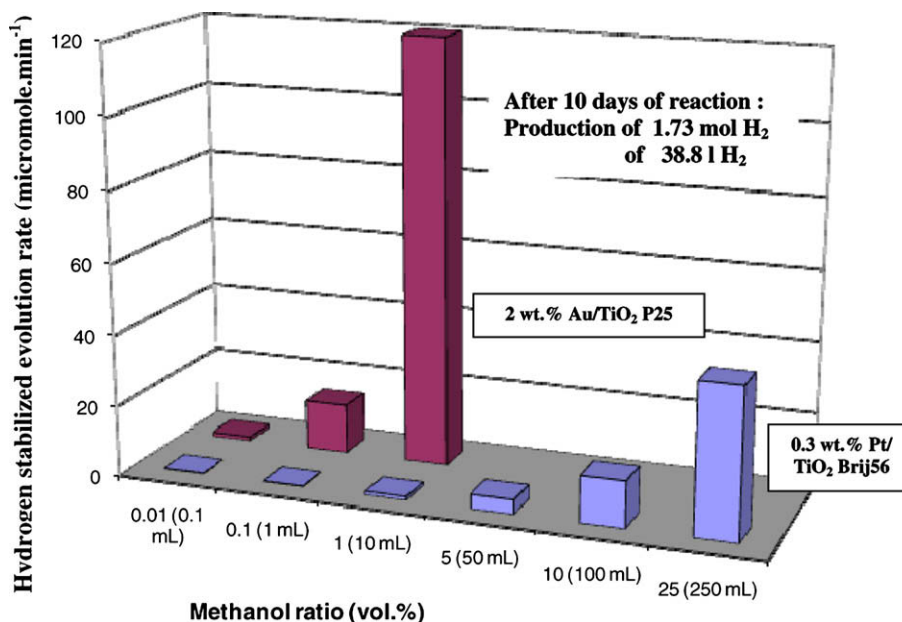
Fig. 11. Comparison of hydrogen evolution rate (mol min^{-1}) on 2 wt.% Au/TiO$_2$–P25 and 0.3 wt.% Pt/TiO$_2$–Brij56 photocatalysts as a function of the relative ratio of methanol sacrificial reagent. Stabilized value over more than 42 h of reaction.

Table 6
Reaction products continuously detected on 2 wt.% Au/TiO$_2$–P25 photocatalyst during the stabilization period under artificial solar light illumination.

Amount of methanol added (mL)	H$_2$ (μmol/min)	O$_2$ (μmol/min)	CO$_2$ (μmol/min)
0.1	1.1	/	0.4
1	14	5.4	2.8
10	120	70	18

(4)). Its presence in the exhaust gas also confirms that methanol does not scavenge all the photogenerated holes.

$$H_2O + 2h^+ \rightarrow 2H^+ + O_2 \qquad (4)$$

Methanol is consumed by two reactions: (i) methanol reforming, which consumes holes and produces H$_2$ and CO$_2$ and (ii) O$_2$ scavenging leading to H$_2$O and CO$_2$. Nevertheless, the detection of O$_2$ proves that under illumination, more holes and O$_2$ molecules are produced than methanol (at this concentration) can scavenge.

It must also be mentioned that in the case of methanol reforming, metal sites poisoning by CO is also to be expected, since it is known that CO strongly adsorbs on noble metals. Nevertheless, CO should also easily be oxidized and released as CO$_2$ under illumination in the presence of O$_2$.

5. Discussion

From these experiments it is possible to draw a few conclusions regarding the role of the metallic co-catalyst and the peculiar behavior of gold nanoparticles supported on TiO$_2$ anatase–rutile support, either commercially available or synthesized by porogen-assisted sol–gel method.

It has been clearly evidenced that the highest H$_2$ production activity was obtained with Au as a co-catalyst deposited on TiO$_2$–P25. Pt-based photocatalysts are less active, whatever the support be. There are two possible and non-exclusive explanations: (i) Pt is very active (more than gold) toward the reverse reaction H$_2$ + ½ O$_2$ → H$_2$O even at room temperature, thus decreasing the efficiency of H$_2$ production. Indeed, it has already been

reported by Iwase and colleagues that on NaTaO$_3$:La, the reverse reaction between O$_2$ and H$_2$ was 1500 times less important with gold nanoparticles as a co-catalyst compared to platinum [47], (ii) the importance of the contact or interaction of the TiO$_2$ semiconductor with the precious metal, this contact depending on the nature of the metallic nanoparticles. Platinum is known to introduce ohmic contact facilitating a quick transfer of electrons to the electrolyte [48]. On the other hand, gold nanoparticles undergo charging and exhibit ability to store and transport electrons at the interfacial semi-conductor (TiO$_2$)–metal composite interface. This charge distribution at the interface results in Fermi level equilibration of the composite. As already reported by Chen and colleagues [49], as gold nanoparticles possess the particular property to undergo quantitized charging, they are unique candidate to achieve Fermi level equilibration. The mediating role of Au nanoparticles for electron storing and shuttling at the TiO$_2$–Au interface, inducing a negative shift in the Fermi level of TiO$_2$, has already been evidenced by Kamat and colleagues [50]. Under illumination, when TiO$_2$ and Au nanoparticles are in contact, the photogenerated electrons are distributed between both kinds of particles, leading to electron transfer from the excited TiO$_2$ to Au, until the two systems attain equilibrium [49,51]. The electron accumulation on the Au particles increases its Fermi level to more negative potentials, also leading to a shift in the Fermi level of the composite closer to the conduction band of the composite. As the Fermi level shifts to more negative potential, the charge separation and reductive power of the Au–TiO$_2$ composite increases, which is of course beneficial to the photocatalytic reduction of H$_2$O into H$_2$. It should also not be forgotten that gold and platinum electrodes are usually reported to display different electrochemical properties in the generation of H$_2$ [52,53].

The influence of the gold nanoparticle size on the H$_2$ production efficiency has also been evidenced in our case. As the loading increased from 0.3 to 2 wt.%, the mean particle size increased from 3 to 8 nm, accompanied by an enhancement in the H$_2$ evolution rate. This tendency is contrary to what is generally observed about the size dependence of catalytic properties of gold nanoparticles deposited on titania [54]. Furthermore, since the energy levels in gold nanoparticles are discrete, a greater shift in energy is expected

for smaller size nanoparticles than for the larger ones. The smaller gold particles thus should have induced a greater shift in the apparent Fermi level of the Au–TiO₂ composite [51]. This clearly means that in our case, other factors should also be considered, in addition to the intimate contact or interaction between the metallic and the semi-conductor nanoparticles.

The compared UV–Vis characterizations of TiO₂-supported gold and platinum photocatalysts showed that gold deposition shifted the absorption edge of the photocatalyst, whereas the deposition of Pt did not affect significantly the absorption spectrum. However, this better light absorption in the visible region of the spectrum cannot explain alone the better results obtained with gold-based catalysts; the nature of the TiO₂ support is also of great importance, especially if we consider the poor results obtained on Au/TiO₂–Brij56 compared to the results obtained on Au/TiO₂–P25. Indeed, as from the results reported in part 3.2, Pt/TiO₂–Brij 56 seemed to be the best combination for Pt-based catalysts, one would have expected the same for Au-based photocatalysts. Despite a lower specific surface area, leading theoretically to a poorer distribution of gold and also to lower accessibility of gold particles on the support, Au/TiO₂–P25 showed the best activity, among gold-based catalysts. This is certainly due to the presence and the nature of surface –OH groups of the TiO₂ support, as we know that the anionic exchange used for gold deposition requires a lot of hydroxyl groups for an efficient anchoring of gold complexes. XPS studies of the bare TiO₂–P25 supports revealed that both the relative amount of surface –OH groups and their chemical environment (or interaction with the surrounding atoms) are different on both kinds of support. Furthermore, the important decrease in the proportion of surface–OH groups after gold deposition on TiO₂–P25, but only on this support, evidenced the formation of strong gold complex–surface interactions, required for an efficient gold deposition. As on the TiO₂–Brij56 support, the proportion of surface hydroxyl groups was less affected by gold deposition, a less efficient deposition and anchoring of gold complexes can be supposed.

Other points derived from the suspension of particles in a liquid medium should also be considered: the surface chemistry, the agglomeration, the sedimentation, and the dispersion of the nanomaterials in the methanol/water solution and, as a result, a possible effect on optical properties. Indeed, as the photocatalytic properties in the liquid phase are sensitive to the state of dispersion of TiO₂-based catalysts because of optical property considerations [55], complementary *in situ* characterization should be performed.

One of the key factors may also be related to the anatase/rutile ratio. Since the anatase phase has a higher density of surface hydroxyl groups, the anatase/rutile ratio (80/20 and 50/50 for TiO₂–P25 and TiO₂–Brij56, respectively) may play an important role. Furthermore, as already mentioned in the literature [56], it should also be reminded that the photogenerated active oxygen species are different for rutile and anatase phases in aqueous solutions containing alcohols as scavenger of holes. But another factor that we consider determinant is the isoelectric point (IEP), together with the deposition conditions. Indeed, gold complexes in solution are negatively charged ($[Au(OH)_xCl_{1-x}]^-$, with $0 < x < 4$). From an electronic interaction point of view, the support has thus to be positively charged for the deposition to be efficient. It can be observed from Fig. 12 that the isoelectric point of the tested supports decreases in the order TiO₂–P25 (6.7) > TiO₂–Brij56 (2.4) > TiO₂–PEG (1.8). The IEP is closely linked to the density of surface hydroxyl groups. Since anatase has a higher density of surface hydroxyl groups than rutile, this decrease in the IEP value with increasing rutile content is not a surprise. Consequently, the low IEP of the sol–gel TiO₂–Brj56 and TiO₂–PEG supports requires very low pHs, lower than 2.4 and 1.8, respectively, for an efficient anchoring of gold particles. Furthermore, at pH < 2.4, gold
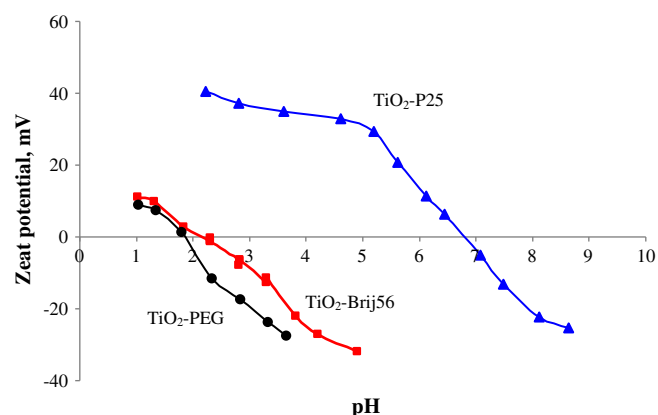

Fig. 12. Zeta potential of TiO₂ P25, TiO₂–Brij56, and TiO₂ anatase–PEG supports.

complexes in solution have a high chloride content ($AuCl_4^-$), the direct anionic exchange is not efficient and the deposited gold particles are prone to sintering.

We can also suppose that the lower activity observed on the TiO₂–Brij56 support mainly results from the deposition method of gold complexes and not from the support itself. Changing the deposition method or using a support with higher anatase/rutile ratio without modifying the large surface area would thus probably lead to higher activities.

We have also put forward the very important role of methanol. Methanol acts as an effective sacrificial reagent by scavenging either O₂ or holes, limiting the reverse H₂ + 1/2 O₂ → H₂O reaction, and increasing charge separation. Even if a part of H₂ is produced by photocatalytic methanol reforming, it has been demonstrated that most of it is issued from direct photocatalytic water splitting.

6. Conclusion

Efficient H₂ production (up to 120 μmol/min) from water splitting using optimal and very small (1 vol.%) amount of methanol has been achieved on low content (0.3 wt.%) Au/TiO₂ anatase–rutile photocatalysts. The addition of methanol is required to reach high evolution rates but keeping this ratio as low as 1 vol.% seems to be a good balance between sustainable high efficiency and limiting the use of fuel-derived and non-renewable resources. The efficiency can be tuned, the main factors affecting H₂ evolution rates are the nature and concentration of the noble metal co-catalyst, the anatase/rutile ratio of the support, its specific area and porosity. In optimized conditions, interesting H₂ production efficiency can be maintained over days without deactivation and without the addition of extra methanol.

References

[1] A. Fujishima, K. Honda, Nature 238 (1972) 37.
[2] Z. Zou, J. Ye, K. Sayama, Nature 414 (2001) 625.
[3] R. Abe, T. Takata, H. Sugihara, K. Domen, Chem. Comm. (2005) 3829.
[4] A. Kudo, Pure Appl. Chem. 79 (2007) 1917.
[5] M. Matsuoka, M. Kitano, M. Takeuchi, K. Tsujimaru, M. Anpo, J.M. Thomas, Catal. Today 122 (2007) 51.

[6] T. Kida, G. Guan, A. Yushida, Chem. Phys. Lett. 371 (2003) 563.
[7] A.L. Linsebigler, G. Lu, J.T. Yates Jr., Chem Rev. 95 (1995) 735.
[8] P. Pichat, New J. Chem. 11 (1987) 135.
[9] G.R. Bamwenda, S. Tsubota, T. Nakamura, M. Hurata, J. Photochem. Photobiol. A: Chem. 89 (1995) 177.
[10] M.C. Blount, J.A. Buchholtz, J.L. Falconer, J. Catal. 197 (2001) 303.
[11] A. Patsoura, D.I. Kondarides, X.E. Verykios, Appl. Catal. B: Environ. 64 (2006) 171.
[12] L.S. Al-Mazroai, M. Bowker, P. Davies, A. Dickinson, J. Greaves, D. James, L. Miljard, Catal. Today 122 (1–2) (2007) 46.
[13] J.G. Highfield, M.H. Chen, P.T. Nguyen, Z. Chen, Energy Environ. Sci. 2 (2009) 991.
[14] A. Sclafani, M.-N. Mozzanega, P. Pichat, J. Photochem. Photobiol. A: Chem. 59 (1991) 181.
[15] N. Strataki, V. Bekiari, D.I. Kondarides, P. Lianos, Appl. Catal. B: Environ. 77 (1–2) (2007) 184.
[16] M. Ashokkumar, Int. J. Hydrogen Energy 23 (1998) 427.
[17] H.-J. Choi, M. Kang, Int. J. Hydrogen Energy 32 (16) (2007) 3841.
[18] J.R. Bolton, Solar Energy 57 (1996) 37.
[19] T. Sakata, J. Photochem. 29 (1985) 205.
[20] F. Bosc, A. Ayral, N. Keller, V. Keller, Appl. Catal. B: Environ. 69 (2007) 133.
[21] F. Bosc, D. Edwards, N. Keller, V. Keller, A. Ayral, Thin Solid Films 495 (2006) 272.
[22] S. Ivanova, V. Pitchon, C. Petit, J. Mol. Catal. A: Chem. 256 (1–2) (2006) 278.
[23] N. Keller, E. Barraud, F. Bosc, D. Edwards, V. Keller, Appl. Catal. B: Environ. 70 (2007) 423.
[24] F. Bosc, A. Ayral, P.-A. Albouy, C. Guizard, Chem. Mater. 15 (2003) 2463.
[25] Y. Kotani, A. Matsuda, M. Tatsumisago, T. Minami, J. Sol–Gel Sci. Technol. 19 (2000) 133.
[26] D. Fattakhova-Rohling, M. Wark, T. Brezesinski, B.M. Smarsky, J. Tathousky, Adv. Funct. Mater. 17 (2007) 123.
[27] T. Klimnova, E. Carmona, J. Ramirez, J. Mater. Sci. 33 (1998) 1981.
[28] H. Liu, J. Yuan, W.F. Shangguan, Energy Fuel 20 (2006) 2289.
[29] V. Keller, P. Bernhardt, F. Garin, J. Catal. 215 (2003) 129.
[30] O. Ishitani, C. Inoue, Y. Suzuki, T. Ibusuki, J. Photochem. Photobiol. A 72 (1993) 269.
[31] C.H. Lin, C. Lee, J.H. Chao, C. Kuo, Y. Cheng, W. Huang, H.W. Chang, Y. Huang, M.K. Shih, Catal. Lett. 98 (2004) 61.
[32] T. Sreethawong, S. Yoshikawa, Int. J. Hydrogen Energy 31 (2006) 786.
[33] A. Abe, K. Sayama, K. Domen, H. Arakawa, Chem. Phys. Lett. 344 (2001) 339.
[34] L. Shi, D. Weng, J. Envir. Sci. 20 (2008) 1263.
[35] C.-Y. Wang, R. Pagel, J.K. Dohrmann, D.W. Bahnemann, Compt. Rend. Chim. 9 (5–6) (2006) 761.
[36] T. Ohno, K. Sarukawa, K. Tokieda, M. Matsumura, J. Catal. 203 (2001) 82.
[37] T. Ohno, K. Tokieda, S. Higashida, M. Matsumura, Appl. Catal. A 244 (2003) 383.
[38] K. Komaguchi, H. Nakano, A. Araki, Y. Harima, Chem. Phys. Lett. 428 (2003) 338.
[39] D.C. Hurum, A.G. Agrios, K.A. Gray, T. Rajh, M.C. Thurnauer, J. Phys. Chem. B 107 (2003) 4545.
[40] S. Link, M.B. Mohamed, M.A. El-Sayed, J. Phys. Chem. B 203 (1999) 3073.
[41] P.V. Kamat, J. Phys. Chem. B 206 (2002) 7729.
[42] G. Marci, M. Addamo, V. Augugliaro, S. Coluccia, E. Garcia-Lopez, V. Loddo, G. Marta, L. Palmisano, M. Schiavello, J. Photochem. Photobiol. A 160 (2003) 105.
[43] A. Mills, G. Porter, J. Chem. Soc. Faraday 78 (1998) 3659.
[44] T. Kawai, T. Sakata, J. Chem. Soc. Chem. Comm. (1980) 694.
[45] P. Pichat, J.-M. Herrman, J. Disdier, H. Courbon, M.-N. Mozzagena, Nouv. J. Chem. 5 (1981) 627.
[46] M. Zalas, M. Laniecki, Sol. Energy Mater. Sol. Cells 89 (2005) 287.
[47] A. Iwase, H. Kato, A. Kudo, Catal. Lett. 108 (1–2) (2006) 7.
[48] D.E. Aspnes, A. Heller, J. Phys. Chem. 87 (1983) 4919.
[49] S. Chen, R.W. Murray, J. Phys. Chem.B. 103 (1999) 9996.
[50] V. Subramanian, E.E. Wolf, V. Kamat, T. J. Am. Chem. Soc. 126 (15) (2004) 4943.
[51] S. Chen, R.S. Ingram, M.J. Hostetler, J.J. Pietron, R.W. Murray, T.G. Schaaf, J.T. Khoury, M.M. Alvarez, R.L. Whetten, Science 280 (1998) 2098.
[52] M.W. Breiter, in: W. Vielstich, H.A. Gasteiger, A. Lamm (Eds.), Handbook of Fuel Cells – Fundamentals, Technology and Applications, vol. 2, John Wiley and Sons, 2003, p. 4.
[53] O. Petrii, G. Tsirlina, Electrochimico Acta 39 (11) (1994) 1739.
[54] M. Haruta, Catal. Today 36 (1997) 153.
[55] T.A. Egerton, I.R. Tooley, J. Phys. Chem. B. 108 (2004) 5066.
[56] H. Goto, Y. Hanada, T. Ohno, M. Matsumura, J. Catal. 225 (2004) 223.